Clinical Imaging 56 (2019) 140–145

Contents lists available at ScienceDirect

Clinical Imaging

journal homepage: www.elsevier.com/locate/clinimag

Neuroradiology

Evaluation of a novel reconstruction method based on the compressed sensing technique: Application to cervical spine MR imaging

Yuki Takato[a,*], Hirofumi Hata[a], Yusuke Inoue[b], Keiji Matsunaga[b], Toshimasa Hara[b], Shotaro Komi[a], Ai Nakajima[a]

[a] *Department of Radiology, Kitasato University Hospital, Sagamihara, Kanagawa, Japan*
[b] *Department of Diagnostic Radiology, Kitasato University School of Medicine, Sagamihara, Kanagawa, Japan*

ARTICLE INFO

Keywords:
Magnetic resonance imaging
Compressed sensing
Zero-fill interpolation
Truncation artifact
Gibbs ringing
Cervical spine

ABSTRACT

Compressed sensing-based reconstruction (CSR) is a new magnetic resonance (MR) image reconstruction method based on the compressed sensing (CS) technique. CSR suppresses ringing artifacts from truncated k-space sampling by estimating the high spatial frequency information required to support the acquired k-space data. CSR is intended to replace the existing zero-fill interpolation (ZIP) reconstruction. We investigated the usefulness of the CSR technique by obtaining sagittal T2-weighted images of the cervical spine and phantom images using CSR or ZIP. Our results indicated that the CSR technique reduces truncation artifacts compared to ZIP without prolonging the scan time or impairing image sharpness.

1. Introduction

There are various artifacts in magnetic resonance (MR) imaging, and they may obscure the correct anatomical structures and be misidentified as a disease. Truncation artifact which is one of the artifacts in MR imaging occurs when the high frequency signal in the k-space is not sampled and appears as stripes parallel to the edges of abrupt signal intensity changes. Increasing the number of phase-encoding steps reduces this artifact but prolongs scan times [1,2].

Zero-fill interpolation (ZIP) is a method to increase the k-space data matrix size. ZIP reduces the voxel size and provides visually smoother edges without prolongation of the scan time. In this approach, the data matrix size is increased in all orthogonal directions and then zero-filling is performed [3–5]. ZIP is a method widely used for reconstruction of MR images. However, in the ZIP image, genuine information is insufficient compared with acquiring real data. As a result, truncation artifacts are more visible in the edges of abrupt signal intensity changes than on the original images without ZIP [4].

Compressed sensing-based reconstruction (CSR) is a new MR image reconstruction method using a compressed sensing (CS) [6–8] framework to estimate missing k-space values for reduction of truncation artifacts and noise. The k-space interpolation is performed in an iterative fashion by promoting sparsity in the image or transform domain and enforcing consistency with the sampled k-space [9]. Unlike traditional CS, which aims to suppress incoherent aliasing artifacts from random undersampling [8], CSR suppresses ringing artifacts from truncated k-space sampling. Ultimately, truncation artifacts are reduced by estimating the high spatial frequency information required to support the acquired k-space data. CSR is intended to replace the existing ZIP reconstruction.

MR imaging of the spine is particularly susceptible to truncation artifacts due to its relatively small diameter and abrupt transitions among the spinal cord, cerebrospinal fluid, and vertebrae. Truncation artifacts are routinely visible inside the spinal cord and vertebral bodies on sagittal T2-weighted images of the cervical spine, and artifacts may interfere with visual image interpretation [1,2,10,11]. In this study, CSR was applied to sagittal T2-weighted fast spin echo imaging of the cervical spine in human volunteers. In addition, a phantom experiment was performed to examine the characteristics of CSR. Our aim was to evaluate the usefulness of the CSR technique for the reduction of truncation artifacts.

2. Materials and methods

2.1. Imaging procedures

All examinations were performed on a 3-Tesla clinical scanner (Discovery 750w DV25; GE Healthcare, Waukesha, WI, USA). Human

---

[*] Corresponding author at: Department of Radiology, Kitasato University Hospital, 1-15-1 Kitasato, Minami-ku, Sagamihara, Kanagawa 252-0375, Japan.
E-mail addresses: ytakato@kitasato-u.ac.jp (Y. Takato), kmri@kitasato-u.ac.jp (H. Hata), kgmatsu@kitasato-u.ac.jp (K. Matsunaga), t-hara@kitasato-u.ac.jp (T. Hara), komi.s@kitasato-u.ac.jp (S. Komi).

https://doi.org/10.1016/j.clinimag.2019.04.005
Received 27 November 2018; Received in revised form 6 April 2019; Accepted 11 April 2019
0899-7071/ © 2019 Elsevier Inc. All rights reserved.

and phantom studies were conducted with a 19-channel phased-array surface coil and a 32-channel phased array coil, respectively. The scan parameters were identical between the human and phantom studies. Images were acquired using a sagittal T2-weighted 2D fast spin echo sequence. Images were acquired using two different acquisition matrices: frequency-encoding matrix (N_x) × phase-encoding matrix (N_y) = 512 × 256 and 512 × 192. Other scan parameters were as follows: repetition time = 4000 ms, effective echo time = 102 ms, echo train length = 14, receiver bandwidth = ± 62.5 kHz, number of excitations = 2, field of view (FOV) = 22 cm × 22 cm, slice thickness/gap = 4.0/1.0 mm, number of slices = 11. The data acquisition times using N_y = 192 and N_y = 256 were 2 min and 2 min 48 s, respectively. The FOV included the posterior cranial fossa and whole cervical spine. The frequency-encoding direction and phase-encoding direction were set in the superior-to-inferior direction and anterior-posterior direction, respectively. In phantom imaging, the frequency-encoding direction and phase-encoding direction were set parallel and orthogonal to the slit in the phantom, respectively.

2.2. Image reconstruction

All acquired data were reconstructed to 512 × 512 matrix images using ZIP or CSR. True spatial resolution was $0.43 \times 1.15\,\text{mm}^2$ in the images acquired using N_y = 192 and $0.43 \times 0.86\,\text{mm}^2$ in the images acquired using N_y = 256. Reconstructed spatial resolution was $0.43 \times 0.43\,\text{mm}^2$ in all images. The ZIP reconstruction represented the standard, commercially available image reconstruction, consisting of apodization filtering and zero-padding. CSR, the investigational reconstruction supplied by the vendor, employed an iterative reconstruction immediately following the coil combine. The reconstructed image (m) was determined by solving the following convex optimization problem:

$$\underset{m}{\text{argmin}}\ \|F_u - k\|_2^2 + \lambda_1\ \|\Psi_m\|_1 + \lambda_2 \text{TV}(m)$$

where F_u is the combined discrete Fourier transform and k-space selection operator, k is the acquired data in the center of k-space, Ψ is a wavelet transform, and TV is the total variation operator. The regularization terms λ_1 and λ_2 were used to adjust the amount of noise reduction. The images were solved with a non-linear conjugate gradient optimization using 125 iterations. CSR images were reconstructed with three levels of noise reduction: (1) no noise reduction (CSR-No), which consisted of a data consistency step after convex optimization; (2) moderate noise reduction (CSR-Moderate); and (3) strong noise reduction (CSR-Strong).

2.3. Human subjects

The study subjects were 12 healthy adult volunteers (6 men and 6 women) aged 25.2 ± 1.9 [mean ± standard deviation (SD)] years, who had no history of chronic disease and no contraindication to MR imaging. The study protocol was approved by the institutional review board, and written informed consent was obtained from all subjects before participation.

2.4. Visual assessment of the striped artifacts level

The five image sets that were used to evaluate the level of striped artifacts in images of the human cervical spine were as follows: ZIP images acquired using N_y = 192 (ZIP-192 images) and 256 (ZIP-256 images), CSR-No images acquired using N_y = 192 (CSR-No-192 images), CSR-Moderate images acquired using N_y = 192 (CSR-Moderate-192 images), and CSR-Strong images acquired using N_y = 192 (CSR-Strong-192 images). The midsagittal slice image was evaluated. Two board-certified radiologists performed visual evaluations of the striped artifacts levels independently, and discrepancies were resolved by consensus between them. The five image sets in each subject were displayed simultaneously on a picture archiving and communication system viewer (EV Insite; PSP Corp, Tokyo, Japan). The display order of the images was randomly rearranged for each subject. The observers were blinded to the image reconstruction methods. Striped artifact levels were evaluated separately in two areas: the spinal cord and vertebral bodies. The observers assigned a score using a 3-point scoring system where 1 = negligible; 2 = mild; and 3 = severe. In sagittal T2-weighted images of the cervical spine, cerebrospinal fluid flow and body motion also cause linear artifacts along the cervical spine [10] and may mimic truncation artifacts. In this study, we assessed the level of striped artifacts and did not attempt to discriminate motion-related artifacts and truncation artifacts.

2.5. Measurement of the signal-to-noise ratio

The signal-to-noise ratio (SNR) in images of the human cervical spine was measured for the following eight image sets: ZIP-192 images, ZIP-256 images, CSR-No-192 images, CSR-Moderate-192 images, CSR-Strong-192 images, CSR-No images acquired using N_y = 256 (CSR-No-256 images), CSR-Moderate images acquired using N_y = 256 (CSR-Moderate-256 images), and CSR-Strong images acquired using N_y = 256 (CSR-Strong-256 images). On the midsagittal slice, the circular regions of interest (ROIs) were placed in the pons and background area behind the pons (Fig. 1). The background ROI was placed avoiding artifacts. The mean signal in the pons ROI was divided by the SD for the background ROI to obtain the SNR.

2.6. Phantom study

A phantom study was performed using the MR imaging phantom (Model 90–401 System II; Nikko Fines, Tokyo, Japan). The phantom was filled with polyvinyl alcohol (PVA) gel and contained a 1 mm thick rectangular acrylic plate as a slit (Fig. 2). The profile curves of the signal intensity were generated using ImageJ software (ver. 1.50i, National Institutes of Health, Bethesda, MD, USA) for the following five image sets: ZIP-192 images, ZIP-256 images, CSR-No-192 images, CSR-Moderate-192 images, and CSR-Strong-192 images. The image sets were prepared to correspond to the sets of visual assessment. A rectangular ROI (frequency-encoding direction × phase-encoding direction = 10 × 100 pixels) was placed across the acrylic slit, and the signal value of each pixel was measured. The signal values of 10 pixels arrayed in the frequency-encoding direction were averaged, and a profile curve representing the signal fluctuation in the phase encoding direction was created. Gaussian fitting was applied to the profile curve around the lowest signal using Origin 2017 software (OriginLab, Northampton, MA, USA), and the full width at half maximum (FWHM)

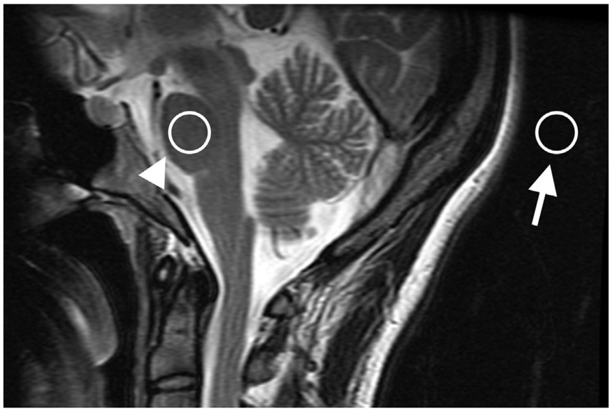

Fig. 1. ROIs placed in the pons (arrowhead) and background area (arrow) for SNR measurement.

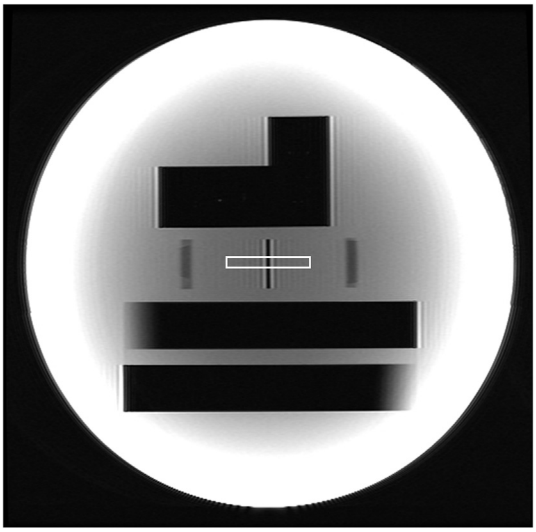

Fig. 2. Phantom image showing the ROI (white rectangle) used for the creation of the profile curve. The frequency-encoding direction and phase-encoding direction were set parallel and orthogonal to the slit in the phantom, respectively.

was calculated as an index of image sharpness.

2.7. Statistical analysis

Values are expressed as means ± SD. The SNRs were compared using repeated measures analysis of variance, and paired *t*-test with Holm correction was used for post-hoc analysis. Striped artifacts scores were compared using the Friedman test, and the Wilcoxon signed-rank test with Holm correction was used for post-hoc analysis. Cohen κ statistics were used to assess inter-observer agreement. A P value < 0.05 was deemed to indicate statistical significance.

3. Results

Table 1
Visual assessment scores for the human images (mean ± SD).

	Spinal cord	Vertebral bodies
ZIP-192	2.58 ± 0.51	1.92 ± 0.51
ZIP-256	1.83 ± 0.72	1.58 ± 0.67
CSR-192-No	1.42 ± 0.51 †	1.08 ± 0.29 †
CSR-192-Moderate	1.42 ± 0.51 †	1.08 ± 0.29 †
CSR-192-Strong	1.50 ± 0.52 †	1.08 ± 0.29 †

The symbol † indicates a statistically significant difference versus ZIP-192 ($p < 0.05$).

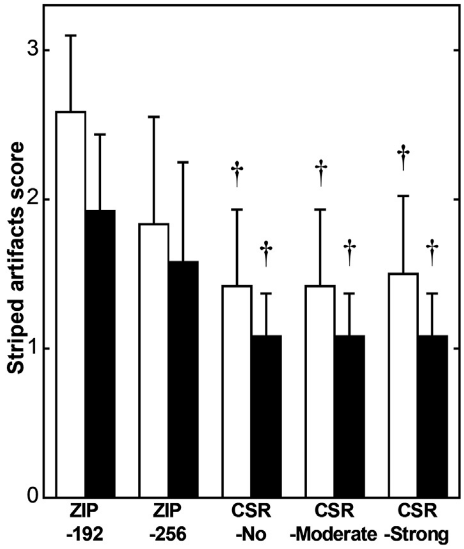

Fig. 4. Visual assessment scores for the human images. The white and black bars represent the results for the spinal cord and vertebral bodies, respectively. The error bars indicate SDs. All CSR images were acquired using $N_y = 192$. The symbol † indicates a statistically significant difference versus ZIP-192 ($p < 0.05$).

Examples of images of the human cervical spine are presented in Fig. 3. In both the spinal cord and vertebral bodies, striped artifact scores were higher for the ZIP-192 images than for the ZIP-256 images (Table 1, Fig. 4) with no statistical significance. Scores were

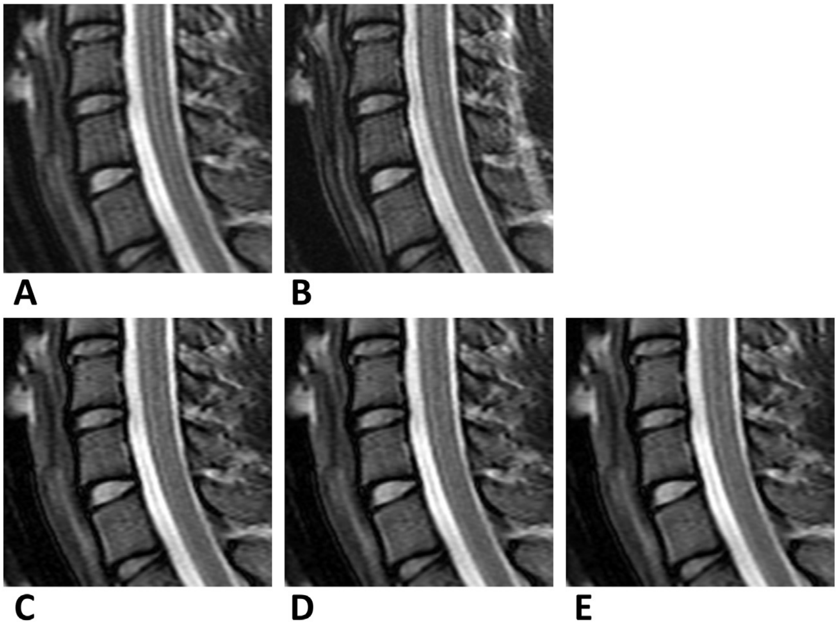

Fig. 3. T2-weighted sagittal images of the cervical spine. ZIP-192 (A), ZIP-256 (B), CSR-No-192 (C), CSR-Moderate-192 (D), and CSR-Strong-192 (E) images are presented.

Table 2
SNRs for the human images (mean ± SD)

	512 × 192	512 × 256
ZIP	30.99 ± 3.28	22.48 ± 3.85
CSR-No	29.28 ± 3.19	20.45 ± 6.07
CSR-Moderate	34.85 ± 4.34‡	23.46 ± 8.21†
CSR-Strong	42.75 ± 6.34‡*	27.73 ± 11.84†*

The symbols †, ‡, and * indicate statistically significant differences ($p < 0.05$) versus CSR-No, ZIP and CSR-No, and CSR-Moderate, respectively.

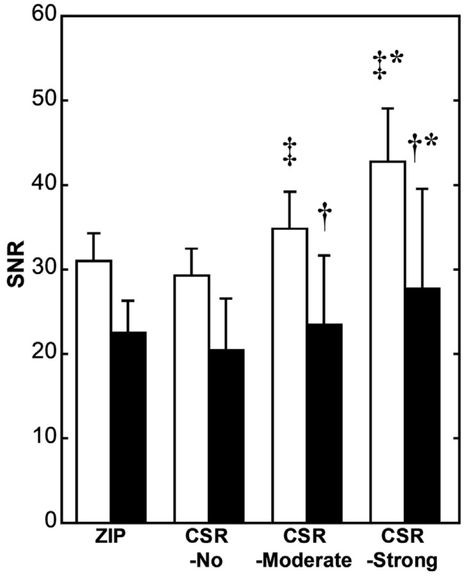

Fig. 5. SNRs for the human images. The white and black bars represent $N_y = 192$ and $N_y = 256$ images, respectively. The error bars indicate SDs. The symbols †, ‡, and * indicate statistically significant differences ($p < 0.05$) versus CSR-No, ZIP and CSR-No, and CSR-Moderate, respectively.

significantly higher for the ZIP-192 images than for the CSR-No-192 images, CSR-Moderate-192 images, and CSR-Strong-192 images. They were also higher for the ZIP-256 images than for the CSR-No-192 images, CSR-Moderate-192 images, and CSR-Strong-192 images, with no significance. They were similar among the three CSR methods. Cohen's kappa statistics indicated moderate inter-observer agreement for the spinal cord (0.435) and substantial agreement for vertebral bodies (0.629).

The SNRs in human images were slightly, but not significantly, lower for the CSR-No images than for the ZIP images (Table 2, Fig. 5). Application of the noise reduction process increased the SNRs in the CSR images. When the SNRs were compared among the images obtained using a phase-encoding matrix of 192, they were significantly higher for the CSR-Moderate-192 images than for the ZIP-192 images and CSR-No-192 images, and for the CSR-Strong-192 images than for the ZIP-192 images, CSR-No-192 images, and CSR-Moderate-192 images. Regarding the images obtained using a phase-encoding matrix of 256, they were higher for the CSR-Moderate-256 images and CSR-Strong-256 images than for the ZIP-256 images, with no statistical significance. They were also significantly higher for the CSR-Moderate-256 images than for the CSR-No-256 images, and for the CSR-Strong-256 images than for the CSR-No-256 images and CSR-Moderate-256 images.

In the phantom studies, the ZIP images showed periodic signal fluctuation parallel to the slit of the phantom (Fig. 6). The signal fluctuation cycle was shorter for the ZIP-256 image than for the ZIP-192 image, but the amplitude of the fluctuation did not differ largely. The signal fluctuation was less evident for the CSR images than for the ZIP images. The signal fluctuation in the CSR images was slightly decreased with stronger noise reduction. Additionally, overshoot appeared on both sides of the slit in all phantom images. The width of the overshoot was slightly narrower for the ZIP-256 image, CSR-No-192 image, CSR-Moderate-192 image, and CSR-Strong-192 image than for the ZIP-192 image. The height of the overshoot was slightly lower for the CSR-Strong-192 image than for the other images. The FWHM around the lowest signal of the profile curve was the smallest for the ZIP-256 image (0.847 mm), followed by the CSR-Strong-192 image (1.021 mm), CSR-Moderate-192 image (1.037 mm), CSR-No-192 image (1.047 mm), and ZIP -192 image (1.104 mm).

4. Discussion

In the present study, we investigated the usefulness of the CSR technique, a new image reconstruction method based on the compressed sensing technique, for reducing truncation artifacts using human and phantom studies. First, we evaluated the level of striped artifacts in cervical spine MR images of human volunteers. The ZIP-192 images, i.e., images with a phase-encoding matrix of 192, displayed evident striped artifacts. These images represented those used in our daily clinical practice. The phase-encoding matrix is usually set to be smaller than the frequency-encoding matrix to shorten the scan time, resulting in predominant truncation artifacts in the phase-encoding direction. One of the ways to reduce truncation artifacts is by increasing the number of phase-encoding steps [1,2,10,11]. In this study, increased phase-encoding steps reduced striped artifacts but without statistical significance. The application of the CSR technique reduced striped artifacts more evidently without prolongation of the scan time. The striped artifacts observed in the ZIP-192 images appear to include motion-related artifacts and truncation artifacts. Motion-related artifacts would not vary between the ZIP and CSR images, and the reduction in striped artifacts is considered to be attributable to that in truncation artifacts. It is indicated that the CSR technique allows for a reduction in truncation artifacts without prolonging scan time and increasing the burden on patients. It will also help radiologists and radiological technologists.

In imaging the cervical spine using a given phase-encoding matrix size, SNRs were slightly lower for the CSR-No images than for the ZIP images. They were elevated for the CSR-Moderate images, and even more elevated for the CSR-Strong images, indicating that improvement of noise properties can be achieved by incorporating noise reduction processing into CSR. Because striped artifact scores did not differ significantly among the three CSR methods, it is considered that the noise reduction processing did not contribute to the reduction of truncation artifacts.

The ZIP images of the phantom demonstrated periodic signal fluctuation parallel to the slit of the phantom, representing truncation artifacts. Although the increase in the phase-encoding steps, from 192 to 256, did not change the amplitude of the signal fluctuation, it shortened the cycle of the signal fluctuation, which appears to be related to the reduction of striped artifacts seen in the images of the human cervical spine. The application of the CSR technique decreased the signal fluctuation more evidently. Similar to the cervical spine images, the phantom studies indicate that the CSR technique reduces truncation artifacts more effectively than increasing the number of phase-encoding steps. The incorporation of noise reduction processing into CSR decreased the signal fluctuation slightly; however, the effect was slight and was not evident in human studies.

When the phantom was imaged using the same acquisition matrix, the FWHM around the lowest signal of the profile curve was smaller in the CSR images, indicating better image sharpness than in the ZIP image. The conventional method to reduce truncation artifacts is windowing with an apodizing filter, such as a Fermi, Hanning or Gaussian filter, to smooth the edges of acquired raw data in the k-space domain, in addition to increasing the acquisition matrix size. However, windowing with an apodizing filter involves a tradeoff between reducing

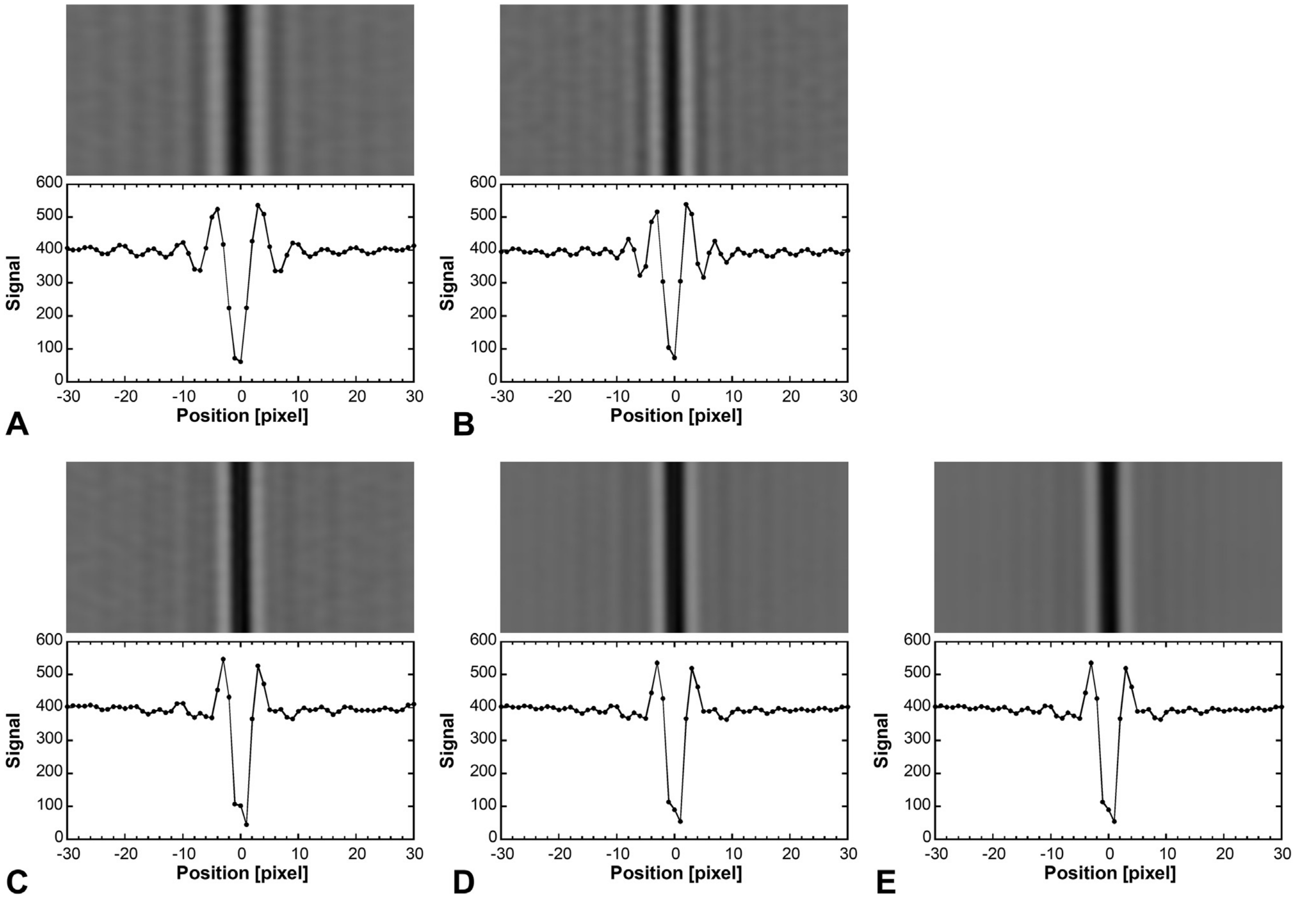

Fig. 6. Phantom images around the slit (upper) and profile curves of the phantom images (lower). The position zero of profile curves was set at the center of the slit. ZIP-192 (A), ZIP-256 (B), CSR-No-192 (C), CSR-Moderate-192 (D), CSR-Strong-192 (E) images are presented.

truncation artifacts and increasing image blur [2,10,12,13]. The CSR techniques can reduce truncation artifacts while maintaining sharpness, in contrast to windowing with an apodizing filter.

Overshoot appeared on both sides of the slit in the phantom images, and remained even after increasing the phase-encoding steps or application of the CSR technique. The overshoot is considered to be caused by Gibbs phenomenon. It has been recognized that Gibbs phenomenon cannot be eliminated even by increasing the acquisition matrix to infinity in mathematics, and is different from truncation artifacts [1]. It is suggested that the CSR technique allows effective reduction of truncation artifacts but not Gibbs phenomenon. However, corresponding artifacts were not demonstrated in images of the human cervical spine.

The results of this study had a limitation. Cohen's kappa statistics indicated moderate inter-observer agreement for the spinal cord (0.435) and substantial agreement for vertebral bodies (0.629). In order to compensate for the low degree of agreement, discrepancies were discussed to establish consensus. However, there were no images to which one of the observers scored 1 and the other scored 3. Statistical confidence may be improved by more observers' assessments.

5. Conclusion

We investigated the utility of the CSR technique using cervical spine MR imaging of human volunteers and phantom imaging. The CSR technique allowed for reduction of truncation artifacts without prolonging the scan time or impairing image sharpness. The results of this preliminary study warrant further investigations of the utility of CSR in patients.

Acknowledgments

We thank Dr. Marc Lebel and Mr. Yuji Iwadate, GE Healthcare, for technical support and helpful discussions and Mr. Hiroki Miyatake, Kitasato University Hospital for his statistical analysis support.

Funding sources

This research did not receive any specific grant from funding agencies in the public, commercial, or not-for-profit sectors.

Conflicts of interest

None.

References

[1] Lufkin RB, Pusey E, Stark DD, Brown R, Leikind B, Hanafee WN. Boundary artifact due to truncation errors in MR imaging. Am J Roentgenol 1986;147:283–7.
[2] Czervionke LF, Czervionke JM, Daniels DL, Haughton VM. Characteristic features of MR truncation artifacts. Am J Roentgenol 1988;151:1219–28.
[3] Du YP, Parker DL, Davis WL, Cao G. Reduction of partial-volume artifacts with zero-filled interpolation in three-dimensional MR angiography. J Magn Reson Imaging 1994;4:733–41.
[4] Parker DL, Du YP, Davis WL. The voxel sensitivity function in Fourier transform imaging: applications to magnetic resonance angiography. Magn Reson Med 1995;33:156–62.
[5] Nakamura T, Naganawa S, Koshikawa T, Fukatsu H, Sakurai Y, Aoki I, et al. High-spatial-resolution MR cisternography of the cerebellopontine angle in 90 seconds with a zero-fill interpolated fast recovery 3D fast asymmetric spin-echo sequence. Am J Neuroradiol 2002;23:1407–12.
[6] Candes E, Romberg JT. Robust uncertainty principles: exact signal reconstruction from highly incomplete frequency information. IEEE Trans Inf Theory 2006;52:489–509.

[7] Donoho D. Compressed sensing. IEEE Trans Inf Theory 2006;52:1289–306.
[8] Lustig M, Donoho D, Pauly JM. Sparse MRI: the application of compressed sensing for rapid MR imaging. Magn Reson Med 2007;58:1182–95.
[9] Smith M, Woehr J, Marasco E, MacDonald ME. Impact of DFT properties on the inherent resolution of compressed sensing reconstructed images. Proceedings of the 24th IET Irish Signals and Systems Conference, Letterkenny. 2013. p. 27.
[10] Vargas MI, Delavelle J, Kohler R, Becker CD, Lovblad K. Brain and spine MRI artifacts at 3Tesla. J Neuroradiol 2009;36:74–81.
[11] Hakky M, Pandey S, Kwak E, Jara H, Erbay SH. Application of basic physics principles to clinical neuroradiology: differentiating artifacts from true pathology on MRI. Am J Roentgenol 2013;201:369–77.
[12] Dietrich O, Reiser MF, Schoenberg SO. Artifacts in 3-T MRI: physical background and reduction strategies. Eur J Radiol 2008;65:29–35.
[13] Veraart J, Fieremans E, Jelescu IO, Knoll F, Novikov DS. Gibbs ringing in diffusion MRI. Magn Reson Med 2016;76:301–14.